ISSN 0038-0946, Solar System Research, 2017, Vol. 51, No. 1, pp. 44–58. © Pleiades Publishing, Inc., 2017.
Original Russian Text © V.V. Shuvalov, V.V. Svettsov, N.A. Artem'eva, I.A. Trubetskaya, O.P. Popova, D.O. Glazachev, 2017, published in Astronomicheskii Vestnik, 2017, Vol. 51, No. 1, pp. 51–66.

Asteroid Apophis: Evaluating the Impact Hazards of Such Bodies

V. V. Shuvalov*, V. V. Svettsov, N. A. Artem'eva, I. A. Trubetskaya, O. P. Popova, and D. O. Glazachev

Institute of Geosphere Dynamics, Russian Academy of Sciences, Moscow, Russia

**e-mail: shuvalov@idg.chph.ras.ru*

Received April 11, 2016

Abstract—Soon after the discovery of asteroid 99942 Apophis, it was classified as a potentially hazardous object with a high probability of an impact on the Earth in 2029. Although subsequent observations have substantially reduced the probability of a collision, it has not been ruled out; moreover, similar-sized asteroids in orbits intersecting the Earth's orbit may well be discovered in the near future. We conduct a numerical simulation of an atmospheric passage and an impact on the Earth's surface of a stony cosmic body with a diameter of 300 m and kinetic energy of about 1000 Mt, which roughly corresponds to the parameters of the asteroid Apophis, at atmospheric entry angles of 90° (vertical stroke), 45°, and 30°. The simulation is performed by solving three-dimensional equations of hydrodynamics and radiative transfer equations in the approximations of radiative heat conduction and volume emission. The following hazards are considered: an air shock wave, ejecta from the crater, thermal radiation, and ionospheric disturbances. Our calculations of the overpressure and wind speed on the Earth's surface show that the zone of destruction of the weakest structures can be as large as 700–1000 km in diameter; a decrease in the flight path angle to the surface leads to a marked increase in the area affected by the shock wave. The ionospheric disturbances are global in nature and continue for hours: at distances of several thousand kilometers at altitudes of more than 100 km, air density disturbances are tens of percent and the vertical and horizontal velocity components reach hundreds of meters per second. The impact of radiation on objects on the Earth's surface is estimated by solving the equation of radiative transfer along rays passing through a luminous area. In clear weather, the size of the zone where thermal heating may ignite wood can be as large as 200 km, and the zone of individual fire outbreaks associated with the ignition of flammable materials can be twice as large. In the 100-km central area, which is characterized by very strong thermal damage, there is ignition of structures, roofs, clothes, etc. The human hazardous area increases with the decrease in the trajectory angle, and people may experience thermal effects at distances of up to 250–400 km from the crater.

Keywords: asteroids, asteroid and comet impact hazard, shock wave, thermal radiation, fires, numerical simulation

DOI: 10.1134/S003809461701004X

INTRODUCTION: ASTEROID APOPHIS

Asteroid 99942 Apophis was discovered at the Kitt Peak National Observatory (Arizona) on June 19, 2004; the object was observed for two consecutive nights and then lost. Six months later the asteroid was rediscovered and immediately became a key matter of concern to specialists and the public because of a very high estimated probability of an impact on the Earth in 2029 (2.6%, or 1 chance out of 38). Subsequent observations of the asteroid eliminated the possibility of an impact on the Earth in 2029, but due to an error in the initial data there was still a possibility of a collision with our planet in 2036 or later.

In 2012–2013, when Apophis made a regular approach to the Earth, there was a rigorous observational campaign using both ground-based and orbiting telescopes (Bancelin et al., 2012; Thuillot et al., 2015), leading to a further refinement of the asteroid's orbital parameters. In 2029, Apophis will fly past the Earth at such a short distance (only 34000–39000 km, or ~5.6 Earth radii, which is close to the altitude of the geostationary orbit, Thuillot et al., 2015) that people in some countries will see it with the naked eye.

After considerable refinement of Apophis's orbit from the observational data, this asteroid is still included in the impact risk table (http://neo.jpl.nasa.gov/risk/index.html) although the probability of its collision with the Earth is very small. As before, there are predictions of encounters with our planet in this century (Sokolov and Kuteeva, 2015). Moreover, it is interesting to evaluate the consequences of a hypothetical Earth impact of an asteroid with the Apophis-like parameters; this is an important research task because many of the bodies that may prove hazardous have not been detected yet.

It is known that an impact of a large space object on the Earth causes a range of hazardous effects (Nemchinov et al., 2005), the scale of which is primarily

determined by the body's kinetic energy, but can also depend (given the same kinetic energy) on the size, speed, flight path angle to the surface, density, and characteristics of the impact site. Delbo et al. (2007) estimated the diameter of the asteroid Apophis from polarimetric observations at 270 ± 60 m. Estimates for the mass and kinetic energy of Apophis are based on a comparison of its IR spectra with those of its possible meteorite analogues and an assumption that Apophis is similar to the asteroid Itokawa. Apophis's mass is estimated at 2×10^{10} kg, and its kinetic energy at entry into the Earth's atmosphere is estimated at 375 Mt TNT (1 t TNT = 4.18×10^9 J) at an entry velocity of 12.6 km/s (Binzel et al., 2009). The thermophysical model by Müller et al. (2014), which is based on the interpretation of observations in the far infrared, yielded a markedly larger diameter (375 m) and a corresponding increase in the mass and energy estimates roughly by a factor of two to four.

When a body with a diameter of 200–400 m (with a kinetic energy of about 1000 Mt) strikes the Earth, the main damaging factors are the shock wave and light radiation. Moreover, an impact of a 300-m object generates acoustic gravity waves and global ionospheric disturbances, which rarely receive sufficient attention (Nemchinov et al., 2005). Harris et al. (2015) estimated that an impact of a 300-m asteroid may cause devastation on a regional scale, and, if the object hits a densely populated area, it may claim millions of human lives. Calculating the exact path of an Earth-impacting asteroid and making the most accurate assessment of the consequences of the impact event are the necessary conditions for a decision to destroy the hazardous object or evacuate the potentially dangerous area. Modern computational methods allow geophysicists to assess the potential hazards of an Earth impact by an Apophis-like asteroid and find out how the zone affected by the shock wave and thermal radiation depends on the flight path angle. In this study, we conducted a numerical simulation of all stages of an impact by a 300-m asteroid at different angles and estimated the overpressure and wind speed at the Earth's surface, thermal radiation fluxes, parameters of the crater, spread of ejecta from the crater, and ionospheric disturbances.

CALCULATION METHOD

The simulation of the processes accompanying an Earth impact of a cosmic body was carried out in three stages. In the first stage, we simulated the motion of the meteoroid in the atmosphere, considering deformation, deceleration, destruction, and evaporation of the body. In so doing, we used the approach described in (Shuvalov and Artemieva, 2002; Shuvalov and Trubetskaya, 2007) and applied, inter alia, to evaluate the consequences of a vertical impact on the Earth of stone asteroids ranging in size from 10 to 300 m (Shuvalov et al., 2013). In this approach, the impacting body is assumed to be quasi-liquid (with a zero resistance), and its deformation under an aerodynamic load is described by equations of hydrodynamics. The rationale for the approximation is that a noticeable deformation of meteoroids larger than a few tens of meters begins at altitudes where aerodynamic loads largely exceed the strength of the falling bodies; therefore, it can be assumed that the body being deformed is completely destroyed at the beginning of the deformation process (Svetsov et al., 1995). Moreover, many large asteroids, including, possibly, Apophis (Müller et al., 2014), are heavily fragmented rubble-pile asteroids.

In the first stage of the simulation, we used a coordinate system associated with the falling body, which is blown around by air. The air density in the oncoming flow changes with the atmospheric stratification, and the flow velocity is equal to that of the body. Thus, when the body decelerates, the velocity of the oncoming flow decreases. To simulate the radiative transfer in the meteoric vapor and in air during the flight and destruction of the meteoroid, we used the approximation of radiative heat conduction. The Rosseland radiation mean free paths for air at typical temperatures behind the front of the head shock wave (1–5 eV) are 1 m or less at altitudes below 30–40 km (Avilova et al., 1970); therefore, this approximation is applicable to large meteoroids. The radiation incident on the body causes its evaporation. The pressure of the incoming vapor is assumed to be equal to that of the gas near the body's surface, and the vapor temperature and density are determined from the phase equilibrium curve. The first-stage calculations ended when the meteoroid reached the Earth's surface.

The resulting distributions of the gas-dynamic and thermodynamic parameters were used as initial data in the second stage of the calculations. In this stage, we used a coordinate system associated with the Earth's surface to simulate the impact cratering, interactions of the ejecta with the atmosphere, and shock wave propagation over long distances. The two stages of the calculations were implemented using the SOVA numerical hydrocode (Shuvalov, 1999). Regardless of the flight path angle, a three-dimensional problem was solved in the second stage. In the three-dimensional problem, radiative transfer was considered in the approximation of radiative heat conduction at altitudes of up to 80 km and in the approximation of volume emission at low optical thicknesses at high altitudes.

The impact cratering calculations considered the effects of dry friction on the motion of rocks destroyed by the shock wave (Melosh and Ivanov, 1999) and used the acoustic fluidization model (Ivanov and Turtle, 2001). Moreover, the condensed ejecta from the crater was transformed into discrete particles whose further motion was described within the standard equations of multiphase gas dynamics, considering the interactions

of the particles with the surrounding air and the target and projectile vapor (Shuvalov, 2003; Shuvalov and Dypvik, 2013).

In the third stage, the calculated parameters of the atmospheric plume (a stream of vapor and solid fragments ejected from the crater and generating a shock wave in the air) were used to simulate the emerging ionospheric disturbance. In this case, we considered an area 9000 km in radius and 1600 km in altitude, neglecting the Earth's sphericity. It should be noted that the equilibrium gas dynamics equations used in the simulation do not describe the motion of air at altitudes above 400–500 km, where the mean free path of molecules is compared with the characteristic height of the atmosphere. Nevertheless, the area of calculations was extended, purely formally, up to an altitude of 1600 km to avoid the use of any artificial boundary conditions at the upper boundary. To calculate the propagation of waves at altitudes of 100–300 km, we replaced the Euler equations by the Navier–Stokes equations, which consider the effects of the molecular viscosity of air since this parameter plays a very important role in the upper atmosphere.

The temperature and density distribution in the undisturbed atmosphere was consistent within the CIRA (COSPAR International Reference Atmosphere) model. The dynamic viscosity of air was assumed to be constant (independent of the density and temperature) at 1.7×10^{-5} Pa s. The calculations used the tables of the equation of state and air radiation mean free paths (Kuznetsov, 1965; Avilova et al., 1970) for H chondrite (Kosarev, 1999, 2009) and the ANEOS equation-of-state tables (Thompson and Lauson, 1972) with the initial data for dunite and quartz (Melosh, 2007).

The temperature and density distributions obtained in the first and second stages of the calculations were used to calculate radiation fluxes at the Earth's surface. The fluxes were calculated by integrating the equation of radiative transfer along rays passing through a luminous area with a temperature above 500 K; the integration was performed in the direction towards the Earth, beginning from cold air towards the inside of the luminous area. On the surface, a grid was defined with the origin at the point of intersection of the body's flight path with the Earth; rays were drawn from the grid nodes at different angles to the surface to take into account the curvature of the Earth's surface. The number of rays passing through the high-temperature area was 6400 (80 rays in each of the two angular directions). The air and vapor temperatures and densities on the ray were obtained by interpolation from the nodes of the difference grid used in hydrodynamic calculations. Along the ray we solved an equation of radiative transfer of the following form

$$\frac{\mathrm{d}I_\varepsilon}{\mathrm{d}s} + k_\varepsilon I_\varepsilon = k_\varepsilon B_\varepsilon, \qquad (1)$$

where I_ε is the spectral intensity of radiation; ε is the energy of quanta; s is the distance along the ray; B_ε is the Planck function; and k_ε is the radiation absorption coefficient. When performing the integration towards the inside of the luminous are, we put the boundary condition $I_\varepsilon = 0$ on the ray's end that was outside the luminous area.

The dependence of I_ε on ε was considered in a multigroup approximation, which was tested previously in simulations of powerful explosions in the atmosphere (Svettsov, 1994a; 1994b). We selected 23 groups by the energy of quanta (Svettsov, 1994a), with both Planck- and Rosseland-averaged absorption coefficients being used in the groups. The difference in the results was 10% or less. The calculations considered (approximately) the transparency of the atmosphere: in the case of nonheated air, we added to the absorption coefficient, which was calculated in the tables without scattering and was very small in the visible area, the extinction coefficient k_{ext}, which depends on scattering and was estimated by Koschmieder's formula (1925):

$$k_{\mathrm{ext}} = 3.912/x_v, \qquad (2)$$

where x_v is the visibility range in the atmosphere (in units of length).

The total radiation intensity is obtained by summing the radiation intensities across the groups based on the energy of quanta. To derive the radiation flux density q at a given point on the Earth's surface, we need to integrate over the angles the radiation intensity multiplied by the cosine of the angle between the ray and the normal to the surface of the irradiated object. By integrating q with respect to time, we can determine the specific thermal energy supplied to a unit area. These values make it possible to determine the effects caused by incident radiation (ignition of materials, melting, burns, etc.).

ATMOSPHERIC PASSAGE AND CRATERING

We conducted a series of numerical experiments in which we simulated an impact on the Earth's surface of a spherical stone (dunite) asteroid 300 m in diameter with a density of 3.32 g/cm^3 (the equation of state for dunite) and velocity of 20 km/s. The Earth's surface was described by the equation of state for quartz with a density of 2.63 g/cm^3. Although the size of the asteroid in the simulation is smaller than the presumed size of Apophis, we neglected porosity, leading to the fact that the total mass and energy of this body (4.7×10^{10} kg and 9.4×10^{18} J or 2.2 Gt TNT) are close to the estimates by Müller et al. (2014).

Figure 1 shows the density distributions for air, vapor, and the condensed material of the projectile at the time when the asteroid approaches the surface at flight path angles of 30°, 45°, and 90° to the horizontal.

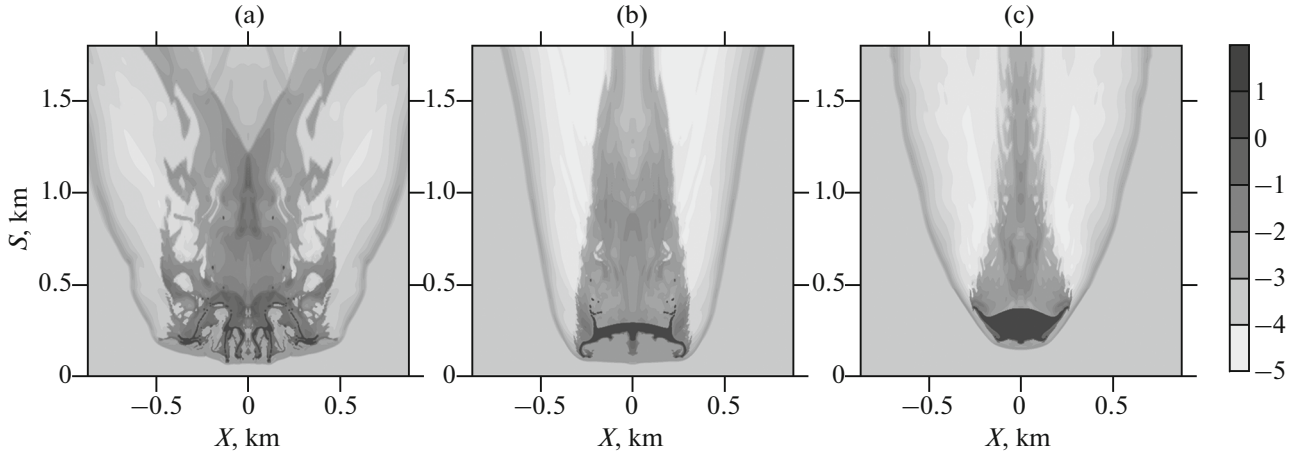

Fig. 1. Flow pattern for a 300-m asteroid at the time of its approach to the Earth's surface at flight path angles of (a) 30°, (b) 45°, and (c) 90°. The figure shows the distributions of the relative density logarithm $\delta = \rho/\rho_a(h)$, where ρ is the density of the material (air, vapor, or body) and $\rho_a(h)$ is the density of unperturbed air at a height of h. The nonevaporated asteroid material is shown in black. The vertical axis plots the distance along the flight path; the horizontal axis plots the distance in a direction perpendicular to the flight path.

In the case of a vertical impact, the 300-m asteroid undergoes deformation, but decelerates only slightly and does not break apart into individual fragments. At a flight path angle of 45°, the asteroid is heavily flattened before the collision with the surface, which is qualitatively consistent with the analytical models proposed by Grigoryan (1979) and Hills and Goda (1993); the area of the asteroid's cross-section increases markedly, and small fragments are separated. At a flight path angle of 30°, the asteroid is heavily fragmented, but the cloud formed by the fragments is rather compact; therefore, the fragmentation has relatively little effect on the crater parameters. In all the cases, the velocity at which the asteroid strikes the surface differs little (by no more than 1%) from that at the atmospheric entry, and this impact leads to cratering.

At flight path angles below 3°–5°, the asteroid may completely evaporate and come to a halt in the atmosphere (Shuvalov and Trubetskaya, 2007). The probability of such impacts is low; therefore, we did not consider this case.

Figure 2 shows the density distributions at different points in time after the asteroid strikes the Earth's surface at an angle of 45°. When passing through the atmosphere, a cosmic body leaves a trail—a hot and rarefied channel. In the case of a vertical impact, the shock wave caused by the scattering of the ejecta from the crater and the wave-heated air propagates mainly along this rarefied channel. In the case of an oblique impact, the initial cratering phase is highly asymmetric: the initial (and the fastest) ejecta fly predominantly in the direction of the projectile's motion; therefore, the impact plume (a cloud of vapor, liquid and solid fragments, and hot air) develops outside the meteor trail. There is also a shock wave along the trail, but this wave is quite weak, resulting only in a slight widening of the trail itself. The initial parameters of the shock wave propagating along the Earth's surface are defined by the interaction of the shock wave arising from the motion of the falling body with the scattering ejecta from the crater. At a late stage ($t > 30$ s), there can be secondary shock waves induced by the fall of the ejecta onto the Earth.

The air temperature in the trail at the time of the impact is 10 kK; that in the head shock wave is even higher. The impact plume from the scattering of the ejecta is much colder; its temperature is close to that of condensation of silicate vapor (about 2 kK).

When a crater is formed after an oblique impact, matter is first ejected in the direction of the impact. When viewed from above, the growing crater has an elongated shape (along the projectile's path). As the crater grows, the asymmetry disappears, leading eventually to a symmetrical circular crater (when viewed from above); however, the center of the crater is displaced relative to that of the impact, i.e., the point of intersection of the flight path with the Earth's surface (by about 1 km at a flight path angle of 45°). Although the asteroid is heavily fragmented and its fragments are scattered near the Earth's surface, the velocity at which the fragments hit the surface is close to that at which the asteroid enters the atmosphere and the crater size is defined mostly by the vertical component of this velocity and depends on the impact angle α approximately as $(\sin\alpha)^\beta$ (where $\beta = 0.3$–0.5, Housen and Holsapple, 2011). The calculations for 45° yielded a crater size of 5.5 km, which is consistent with estimates based on scaling relations (Housen and Holsapple, 2011). Estimates show that in the angle range under study, the diameter of the final complex crater is

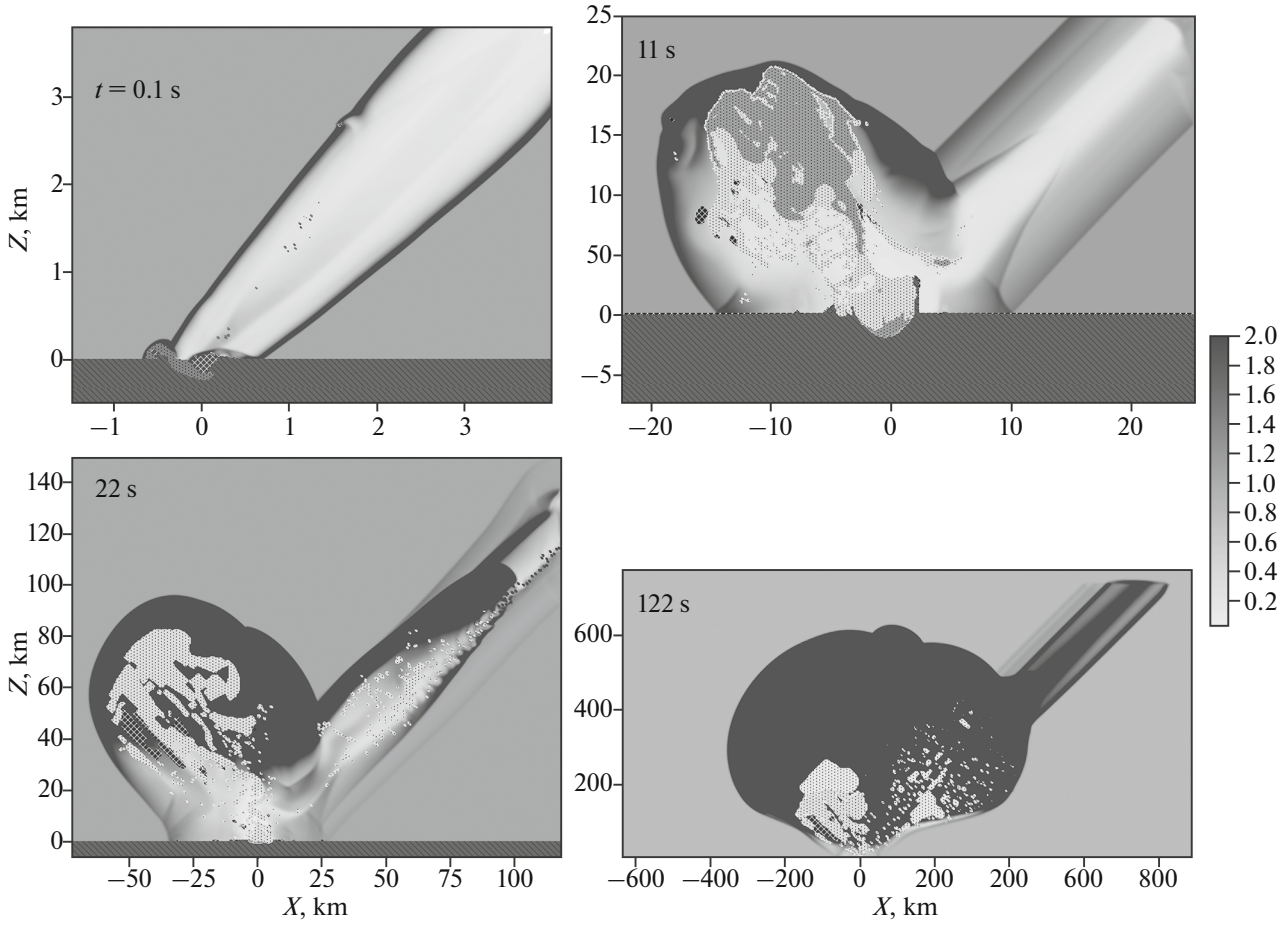

Fig. 2. Density distributions at different points in time after an impact of a 300-m asteroid on the Earth's surface at an angle of 45°. The relative air density is shown by shades of gray (see the scale on the right), ($\delta = \rho/\rho_a(h)$, where ρ is the density of a substance (air, vapor, or body) and $\rho_a(h)$ is the density of unperturbed air at a height of h; the relative densities of the projectile and target material are shown by shades of gray with dots and dashes, respectively. (Unfortunately, we have insufficient graphics capabilities to show the complexity of the flow pattern.)

~4.5 to ~6.5 km (McKinnon and Schenk, 1985) and the average crater depth is about 0.5 km (Herrick et al., 1997).

The total mass of ejecta from the crater for a vertical impact is about 270 M, where M is the mass of the projectile, i.e., 1.3×10^{13} kg. The crater ejecta can be classified, in a first approximation, into ballistic and convective (Shuvalov and Dypvik, 2013). The flight path of ballistic ejecta depends on its initial velocity and, later, on its deceleration in the atmosphere. Convective ejecta loses its initial velocity very fast, and its further movement is fully defined by air currents caused by the projectile's impact and cratering (in the first minutes) and local weather conditions (in the subsequent hours and days). Ballistic ejecta consists of larger particles (above 10 cm); particles of a millimeter size or smaller can be classified as convective ejecta (Shuvalov and Dypvik, 2013).

The thickness of the ejecta layer decreases with the distance from the crater center by the power law (McGetchin et al., 1973; Shuvalov and Dypvik, 2013). The layer is more than 100 m thick near the crater wall, a few meters at a distance of 10 km from the crater center, and ~0.1 m at a distance of 25 km. As is seen from Fig. 2, the impact ejecta from the forming crater can reach large altitudes (100–200 km in 2 min after an impact at 45°; Fig. 2), but the mass fraction of this matter is small. Calculations (Shuvalov and Dypvik, 2013) show that as early as 10 min after a vertical impact, a large portion of the ejecta, including millimeter-sized particles, reaches the surface and forms a deposit layer. Smaller particles (1–10 μm) concentrate mostly below 25 km in altitude; at that time, only 4% of the ejecta (~10 M) remains in the atmosphere. Only a relatively small portion of the tiniest particles can rise to higher altitudes. The vaporized material rises even higher, up to altitudes of 100–150 km, but its relative amount is small, about 0.01 M. The emissions of long-

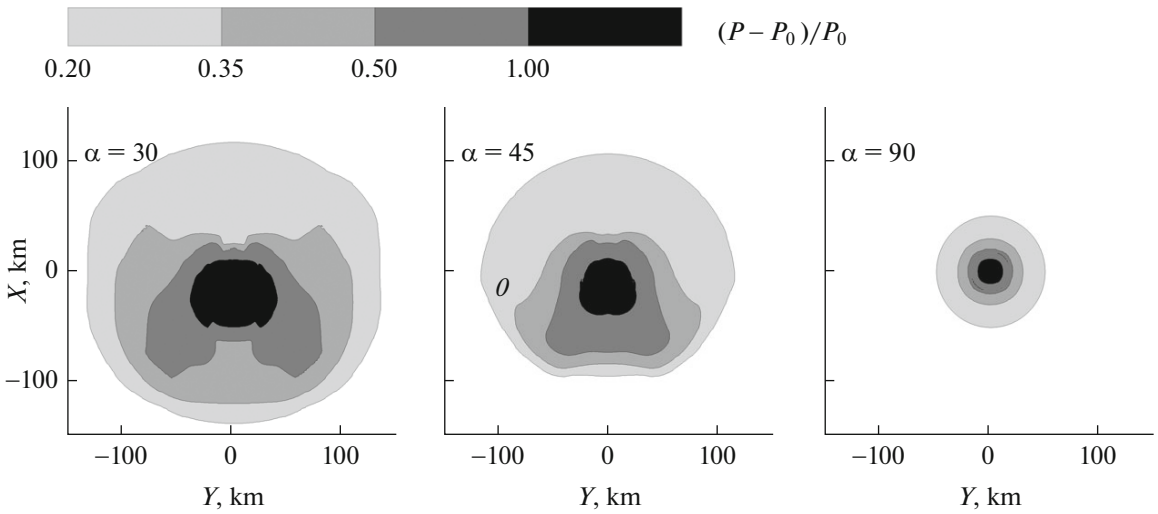

Fig. 3. Distribution of the maximum overpressure on the Earth's for impacts of a 300-m asteroid at different angles α to the surface. In the case of an oblique impact, the asteroid moves downwards (from the area $X > 0$) and touches the surface at the point $X = 0$, $Y = 0$.

lived microparticles into the upper atmosphere together with those of smoke and chemicals from the ensuing fires (see below) may lead to changes in the optical, chemical, and electrical properties of the Earth's atmosphere (an example is the light nights after the Tunguska catastrophe (Vasil'ev, 2004)). However, impacts on the scale of Apophis are not expected to cause long-term weather and climate effects, which have been widely discussed in the literature in the context of volcanic eruptions and fires resulting from a hypothetical nuclear war and an impact of a giant asteroid on the boundary between the Cretaceous and Paleogene (Pittock et al., 1986; Toon et al., 1997; Nemchinov et al., 2005).

OVERPRESSURE AND WIND SPEED ON THE EARTH'S SURFACE

The main characteristic of a shock wave (SW) near the surface is overpressure ΔP with respect to the normal atmospheric pressure P_0 or the dimensionless value $\Delta P/P_0$. Assessments of damage caused by the propagation of an SW are usually based on data obtained from powerful explosions (Glasstone and Dolan, 1977), which show that walls built from concrete blocks (with a thickness of 24–36 cm) are destroyed at an overpressure of $\Delta P = 35$ kPa ($\Delta P/P_0 \sim 0.35$) and brick walls of the same thickness collapse at $\Delta P = 20$ kPa ($\Delta P/P_0 \sim 0.2$).

A widely used approach is to divide the area of destruction into four zones (A, B, C, and D): the mild destruction zone (D) involves damage to windows, wall panels, and roofs and corresponds to an overpressure of 3.5–5 kPa; more serious damage requiring the recovery of more than 50% of structural elements (zone C) occurs at peak pressures above 17–20 kPa; in zone B, buildings are almost completely destroyed at pressures >35 kPa; finally, in the total destruction zone A, the pressure differential exceeds 60–83 kPa (Mannan and Lees, 2005). Overpressure is detrimental to living organisms as well as buildings. The lethality threshold is estimated at about 280 kPa (Mannan and Lees, 2005).

Figure 3 shows, for impacts at different path angles, the areas on the Earth's surface where the maximum overpressure during the impact is above 20, 35, 50, and 100 kPa. It is evident that the damage areas associated with oblique impacts are not symmetrical with respect to the point of intersection of the flight path with the Earth's surface and slightly resemble in shape the forest fall zone at the Tunguska site (Vasilyev, 2004) and the overpressure area in the Chelyabinsk meteoroid event (Popova et al., 2013). The shape of the area where atmospheric overpressure exceeds a certain critical value changes with the change in this value. At large critical overpressures, the area of destruction is not symmetrical and is displaced in the direction of the projectile motion. At small overpressures, the area where they are reached becomes almost symmetrical. The area of very small overpressures is again not symmetrical (see Fig. 5 below). The size of the zone of substantial damage (zone C, $\Delta P/P_0 \sim 0.35$) is about 150 × 220 km^2 for an impact at an angle of 30°, 100 × 180 km^2 at 45°, and 50 × 50 km^2 for a vertical impact.

The decrease in the path angle leads to a dramatic increase, by several times, in the size of the zone bounded by any overpressure. In the case of an oblique impact, we can assume, in a first approximation, that the projectile energy associated with the vertical component of the projectile velocity is spent on cratering

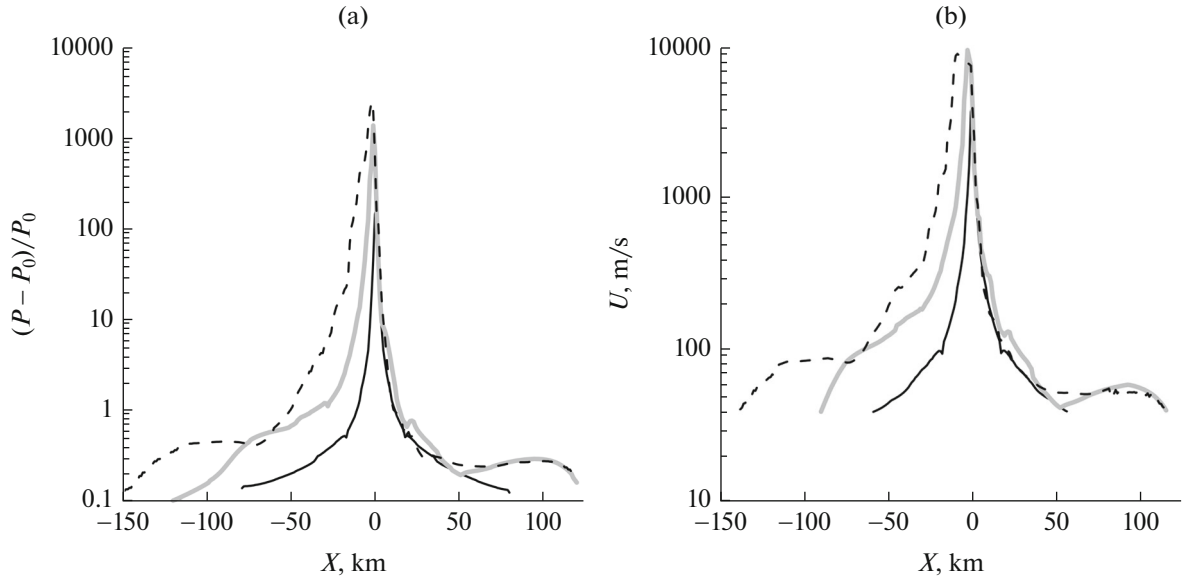

Fig. 4. Distributions of (a) the maximum overpressure and (b) maximum air velocity behind the shock wave front along the X axis, which coincides with the projection of the asteroid's flight path onto the Earth's surface, at different flight path angles. The solid black line corresponds to a vertical impact (90°); the thick gray line, to an impact at 45°; and the dashed curve, to an impact at 30°. In the case of a vertical impact, the velocity on the symmetry axis ($X = 0$) is zero, but this zone is small on the scale used in the figure and is therefore not shown.

and the energy associated with the horizontal component is released in the atmosphere and increases the amplitude of the shock wave. This observation is confirmed by the fact that craters formed by oblique impacts are smaller in size than those formed by vertical impacts (Pierazzo and Melosh, 2000).

Figure 4a shows the distributions of the maximum impact overpressure along the line $Y = 0$ (parallel to the X axis), which coincides with the projection of the asteroid's path onto the Earth's surface (Fig. 3). In the case of oblique impacts, the asteroid moves from the area $X > 0$ downwards and touches the surface at the point $X = 0$. In the area $X < 0$ (in the direction opposite to where the asteroid came from), the smaller the path angle, the larger the overpressure zone. In the case of oblique impacts, at the initial time points, ejecta from the crater and a considerable portion of the projectile material fly in the direction of the asteroid's motion to support the shock wave propagating in this direction. In the area $X > 0$ at distances less than 50 km, overpressures are almost independent of the path angle; at larger distances of about 100 km, oblique impacts induce a stronger SW.

The complex pattern of the dependence of the SW amplitude on time and distance is due to the anisotropy of the cratering process. The initial wave is generated by the asteroid moving in the atmosphere; the further attenuation or acceleration of the SW is controlled by the interaction of the meteor trail with the surface and the scattering of the ejecta, which affects the air medium like a piston. The change in the direction where material is ejected from the crater (first in the direction of the asteroid's motion and then in all directions), the deceleration of the ejecta and its deposition in the gravity field affect the change in the SW intensity in different directions. At a late stage, when the SW is not so strong (i.e., when the overpressure is comparable or less than the normal atmospheric pressure), its amplitude is affected by the atmospheric temperature stratification (the altitude dependence of the velocity of sound).

Figure 4b shows similar data for the distribution of the maximum (with respect to time) horizontal velocities of the airflow on the surface. In contrast to the velocity distributions for impacts of smaller bodies that fully decelerate in the atmosphere, i.e., giant fireballs, such as the Tunguska event in 1908, when the shock wave hits the surface vertically at the epicenter of the airburst, in our case of oblique impacts, there is no zone with zero horizontal velocity (such as the "telegraph forest" zone in the Tunguska event). As with overpressure, the size of the damage area, which is determined from the velocity, increases substantially with decreasing path angle.

It should be noted that the magnitudes of overpressure that cause a given effect are known with inaccuracies and are always estimated approximately. The recent Chelyabinsk meteoroid event caused a large area of destruction (on a territory exceeding 10000–12000 km^2), with damage mainly to windows, suspended ceilings, wall panels, etc.

This area can be classified as zone D; an overpressure of 1000 Pa ($(\Delta P/P_0 \sim 0.01)$ can be considered as

the boundary of the area of mass damage to windows (Popova et al., 2013).

It is evident from Fig. 5 that an impact of a 300-m asteroid at an angle of 45° creates a mild destruction zone (zone D) that can extend to distances of about 350–400 km from the crater, i.e., on an area of about 400000 km^2, which is larger by a factor of 20–40 than in the Chelyabinsk event. The peculiar shape of the mild destruction zone is due to the complex interactions between the shock waves generated during the atmospheric passage and destruction of the meteoroid, cratering, and fall of the material ejected (not isotropically) from the crater onto the Earth (at a late stage, $t > 30$ s).

The lethality threshold is exceeded at a distance of about 15 km from the impact site at an impact angle of 45°.

IONOSPHERIC DISTURBANCES

In addition to destruction on the Earth, Apophis-like asteroids generate global disturbances in the Earth's ionosphere. To estimate the degree of deformation of the atmosphere in the simulation, we evenly distributed passive markers across the area of calculations; the markers were moving with the speed of the airflow after the impact. The shifts of the markers within the first few tens of minutes are shown in Fig. 6. The initial data to calculate the movement of the ionosphere (atmospheric plume parameters) were taken from the impact problem.

The calculations show that at altitudes above 100 km, the atmosphere remains considerably disturbed for several hours within distances of several thousands of kilometers. In addition to oscillations, there is a substantial transfer of material, particularly in the horizontal direction. The maximum shift of the markers is observed at altitudes of about 100 km in an area characterized by a sharp increase in temperature and the speed of sound. Below 100 km the atmosphere is almost undisturbed except for a relatively small area at the epicenter.

The air density disturbances are up to several tens of percent at altitudes above 100 km, and the radius of the disturbed region is 6000–7000 km two hours after the asteroid impact. Analysis of the distributions of the horizontal and vertical velocity components shows that the ejection of material into the upper atmosphere generates a strong acoustic compression wave with an amplitude of more than 100 m/s (horizontal velocity) within about 6000 km from the impact site as late as two hours after the impact. The compression wave is followed by oscillations with a period of 5–10 min and a wavelength of about 100–200 km, which can be interpreted as acoustic gravity waves.

These oscillations are clearly visible in Fig. 7, which shows the time dependences of density and velocity disturbances for a point located at an altitude of 200 km and at a distance of 2000 km from the crater.

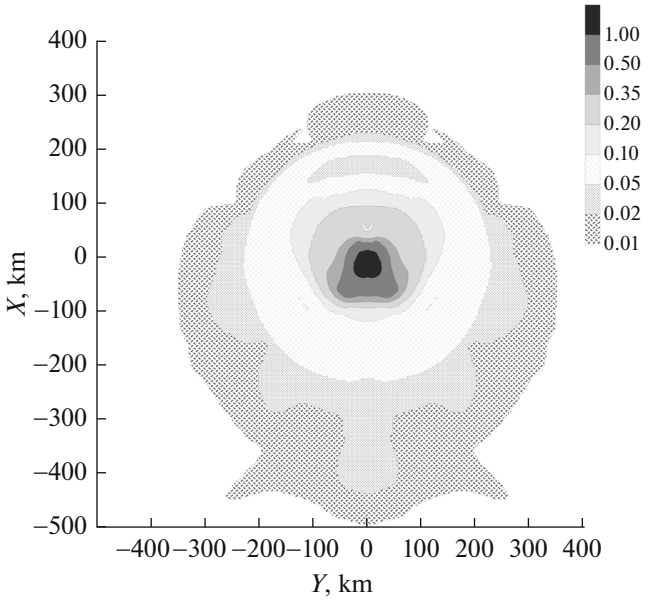

Fig. 5. Distribution of the maximum overpressure ($\Delta P/P_0$; the scale is given in the figure; $\Delta P/P_0 \sim 0.01$ corresponds to an overpressure of 1000 Pa) on the surface for an impact of a 300-m asteroid at a flight path angle of 45°.

The oscillations are most visible in the curve of the vertical velocity component. The maximum oscillation amplitudes are at altitudes of 100–300 km. Above 200 km a substantial contribution comes from the molecular viscosity of air, which reduces the oscillation amplitude despite the exponential decrease in density.

THERMAL RADIATION

The time dependences of the total radiation flux for two values of the impact angle—90° (vertical impact) and 45°—are shown in Fig. 8. Here and below we show the results for a 50-km visibility range in the atmosphere, i.e., for very clear weather, to assess the maximum possible effect.

The calculation starts at the time when the asteroid is at an altitude of 40 km, and time is measured from the moment of its atmospheric entry at an altitude of 120 km. There is an increase in the radiation flux for a few seconds, as the asteroid is approaching the Earth. After the impact on the Earth, the increase in the flux continues for a few more seconds, while there is intense radiation from the trail following the body in the atmosphere. After a vertical impact, vapor is released into the trail and moves upward, expanding and cooling. In approximately 20 s, the flux begins to substantially decrease to drop by two orders of magnitude in 100 s, and the intense radiation stops. In the case of an impact at 45°, vapor is released into the atmosphere outside the trail, i.e., in the direction of the impact. The vapor decelerates in the atmosphere

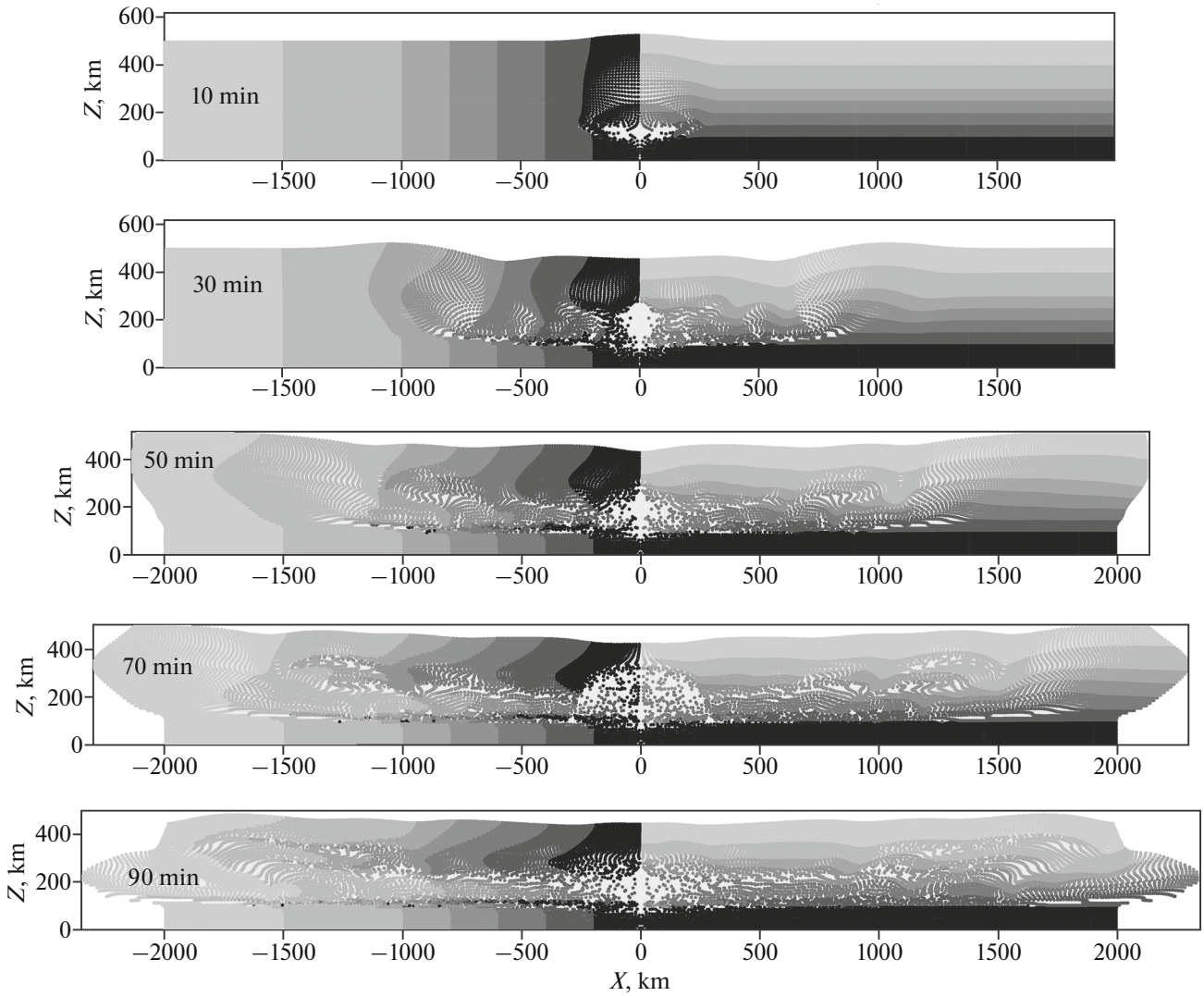

Fig. 6. Distributions of passive markers moving together with gas to demonstrate the disturbance of the atmosphere after a vertical impact on the Earth of a 300-m stone asteroid at a velocity of 20 km/s. Time in minutes from the moment of the impact is indicated in each figure. The initially undisturbed atmosphere is divided into vertical and horizontal layers (at $X > 0$ and $X < 0$, respectively) for a more visual representation of the atmospheric processes.

and radiates during a much longer period, for ~200 s, after which the radiation flux also drops to negligibly small values due to the cooling of vapor and air during the adiabatic expansion, radiation, and mixing. At an angle of 45°, the mass of the released vapor is much higher, which also leads to a longer period of cooling, compared with a vertical impact. Over the entire period of radiation, the Earth's surface receives an amount of energy equal to ~0.6% of the asteroid's initial kinetic energy (2.2 Gt TNT) for a vertical impact and ~4.5% for an impact at 45°.

Whether the impact event leads to a fire depends both on the density of the radiation flux on the irradiated object and on the length of the radiation period, i.e., the energy impinging upon a unit area (specific radiation energy). Highly flammable dry pine needles (forest litter with an average density of 0.006–0.024 g/cm^3) ignite at a radiation flux density no less than 1 W/cm^2, and the time of ignition decreases with increasing average density of the pine needle layer and can be 4–6 s at a density of 0.024 g/cm^3 (Grishin et al., 1999).

Theoretical estimates for the time of ignition of wood by a constant radiation flux, which are based on the solution of the heat conduction equation (Janssens, 1991), give the following relation for the time of ignition

$$t_{ig} = \left(\frac{\lambda \rho C}{h_{eff}^2}\right)\left(\frac{0.73 q_{cr}}{q - q_{cr}}\right)^{1.82}, \qquad (3)$$

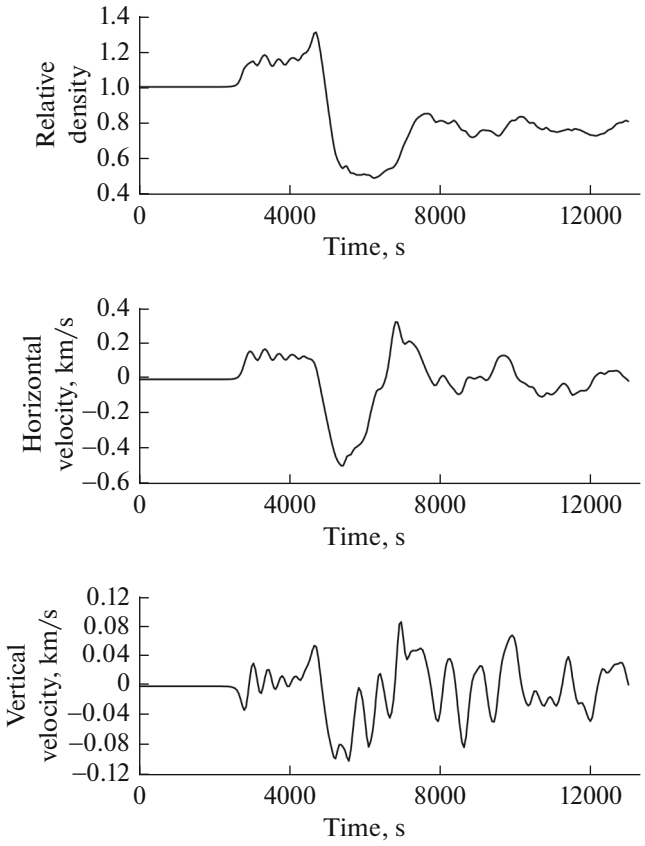

Fig. 7. Time dependences of the relative density (upper panel) and horizontal (middle panel) and vertical (lower panel) velocity components at a height of 200 km and a distance of 2000 km from the site of a vertical impact on the Earth of 300-m stone asteroid at a velocity of 20 km/s.

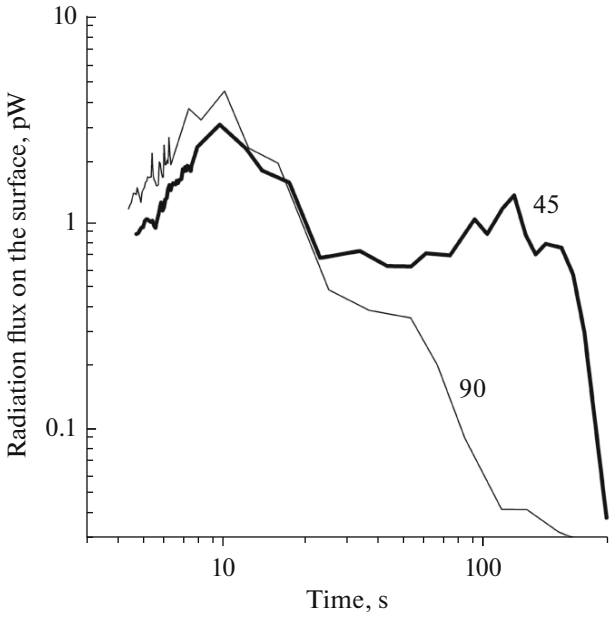

Fig. 8. Time change of the total radiation flux on the Earth's surface for an impact of a 300-m asteroid at angles of 90° and 45° to the horizontal.

where q is the density of the radiation flux; q_{cr} is the critical density of the radiation flux; λ is the coefficient of thermal conductivity; ρ is the density of wood; C is the specific heat; and h_{eff} is the effective coefficient of convection.

Babrauskas (2001, 2003) took characteristic values of the coefficients and reduced this relation to the form

$$t_{ig} = \frac{300\rho^{0.73}}{(q-1.1)^{1.82}}. \quad (4)$$

This relation uses the following measurement units: W/cm^2 for q, g/cm^3 for ρ, and s for t, with the range of densities of wood being 0.17 to 0.85 g/cm^3 and $q > 1.5$ W/cm^2.

The specific energy e (J/cm^2) supplied to the irradiated object during this period is

$$e = qt_{ig} = 1.1t_{ig} + 23\rho^{0.4}t_{ig}^{0.45}. \quad (5)$$

For dry pine wood ($\rho = 0.5$ g/cm^3),

$$e = 1.1t_{ig} + 17t_{ig}^{0.45}. \quad (6)$$

If the radiation flux changes over time (increases, decreases, or first increases and then decreases), the specific energy required for ignition during the time t_{ig} is less than the energy needed for ignition by a constant radiation flux with an average magnitude (Enaleev et al., 2013; Filkov et al., 2014).

Figure 9 shows the distributions of this thermal energy and the radiation flux density on objects on the Earth's surface after a vertical impact of the asteroid. Since the flux density depends on the orientation of the irradiated surface, Fig. 9 shows the flux density and the irradiation energy for surfaces oriented towards the radiation source. In the last case, these are almost vertical objects for large distances. It is these objects that are the first to ignite. Thus, we give here the maximum (by direction) radiation fluxes.

It is evident from Fig. 9 that at distances of about 250 km from the impact site (at the origin of coordinates), the maximum flux density is as high as 1 W/cm^2 and remains at this level for no less than 5 s; at these distances in clear weather, flammable materials such as dry pine needles may ignite (Grishin et al., 1999). Given that radiation acts on wood for 8 s, the specific radiation energy needed to ignite pine wood is estimated from (6) at 50 J/cm^2; considering that the radiation flux is variable (Fig. 8), it is somewhat smaller. Thus, wood may ignite at distances of about 100 km from the center. The impact of the Tunguska cosmic body on June 30, 1908, caused a fire over an area of about 500 km^2 (Vasilyev, 1998), which is four times smaller than the tree fall area due to explosion waves (2000 km^2). An impact of a 300-m asteroid

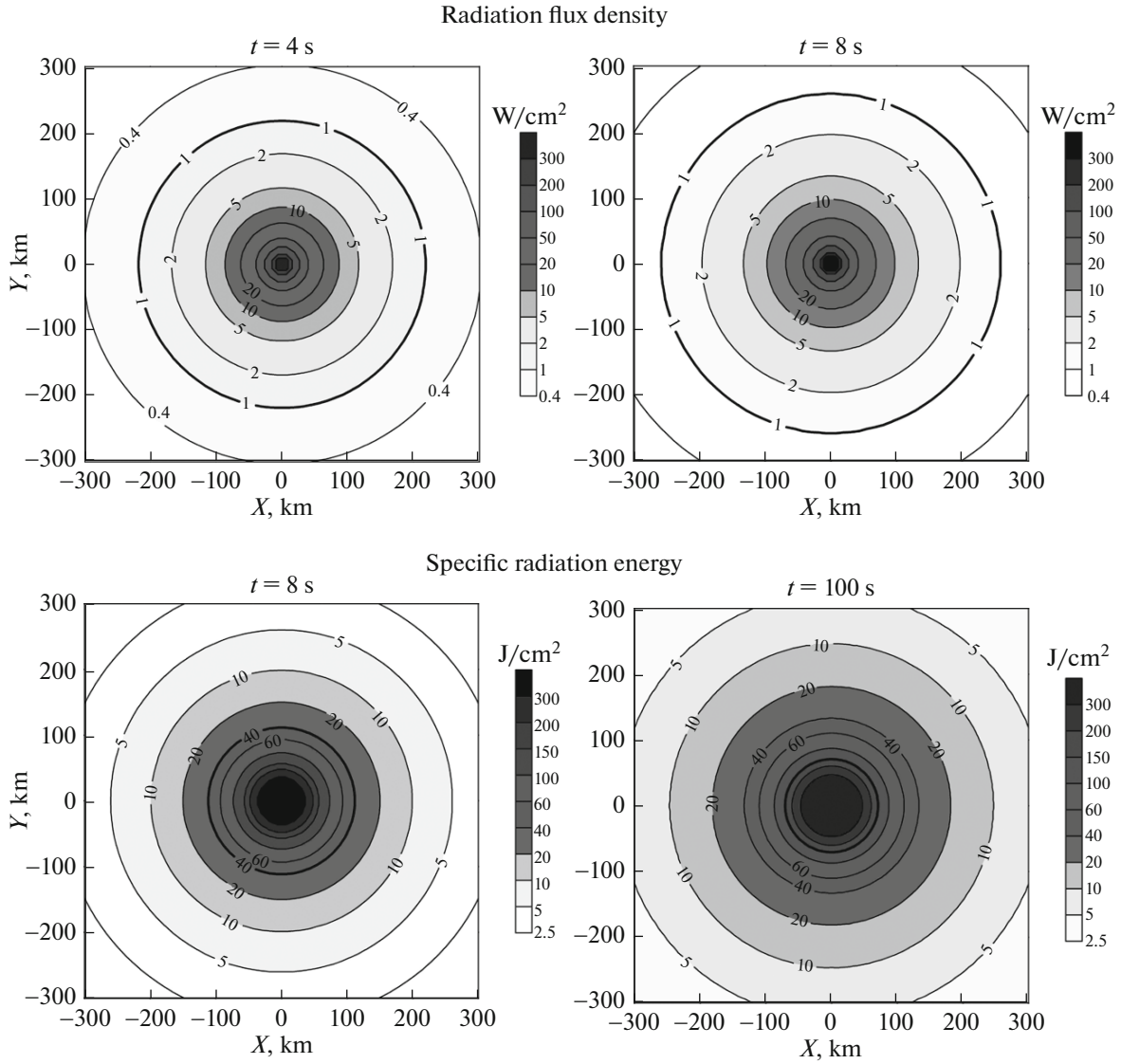

Fig. 9. Isolines of the radiation flux density and specific radiation energy on objects located on the Earth's surface and oriented at the radiation source for a vertical impact of a 300-m asteroid at a velocity of 20 km/s at times of 4, 8, and 100 s. Time is counted from the moment when the asteroid reaches an altitude of 40 m in the atmosphere. The origin of coordinates (*X, Y*) on the Earth's surface is located at the point of intersection of the asteroid's flight path with the Earth.

would cause fires on a much larger scale, i.e., over an area greater than 30000 km^2.

After 100 s, there is no visible increase in the radii of the areas with the maximum radiation energy above a given level; i.e., the main thermal impact occurs during a fairly short time of about 10 s. Similar times of thermal impact are also typical of concentrated explosions with energies of about 10 Mt TNT (Svettsov, 1994b). Based on the data in (Glasstone and Dolan, 1977) for a 20-Mt airburst, fallen leaves and rotten wood ignite at a radiation energy of ~35 J/cm^2, newspapers at ~40 J/cm^2 (i.e., roughly like the above estimates for dry wood), and black rubber at ~100 J/cm^2; at radiation energies above 150–300 J/cm^2, roll roofing ignites, the thin aluminum skin of aircraft covers with blisters, and the soil may begin to melt. Therefore, there is a zone of very high thermal damage within 50 km from the impact site.

Damage to humans from thermal radiation is contingent on the received thermal dose, which depends on the exposure time and intensity approximately as $L = tI^{4/3}$, but different authors give substantially different data on the doses (Mannan and Lees, 2005). A thermal shock causing second-degree burns is about 4–25 J/cm^2, and that causing third-degree burns is 12.5–37.5 J/cm^2. The minimum radiation flux causing pain after a 10-s exposure on human skin is about 0.4 W/cm^2; second-degree burns are caused by a radia-

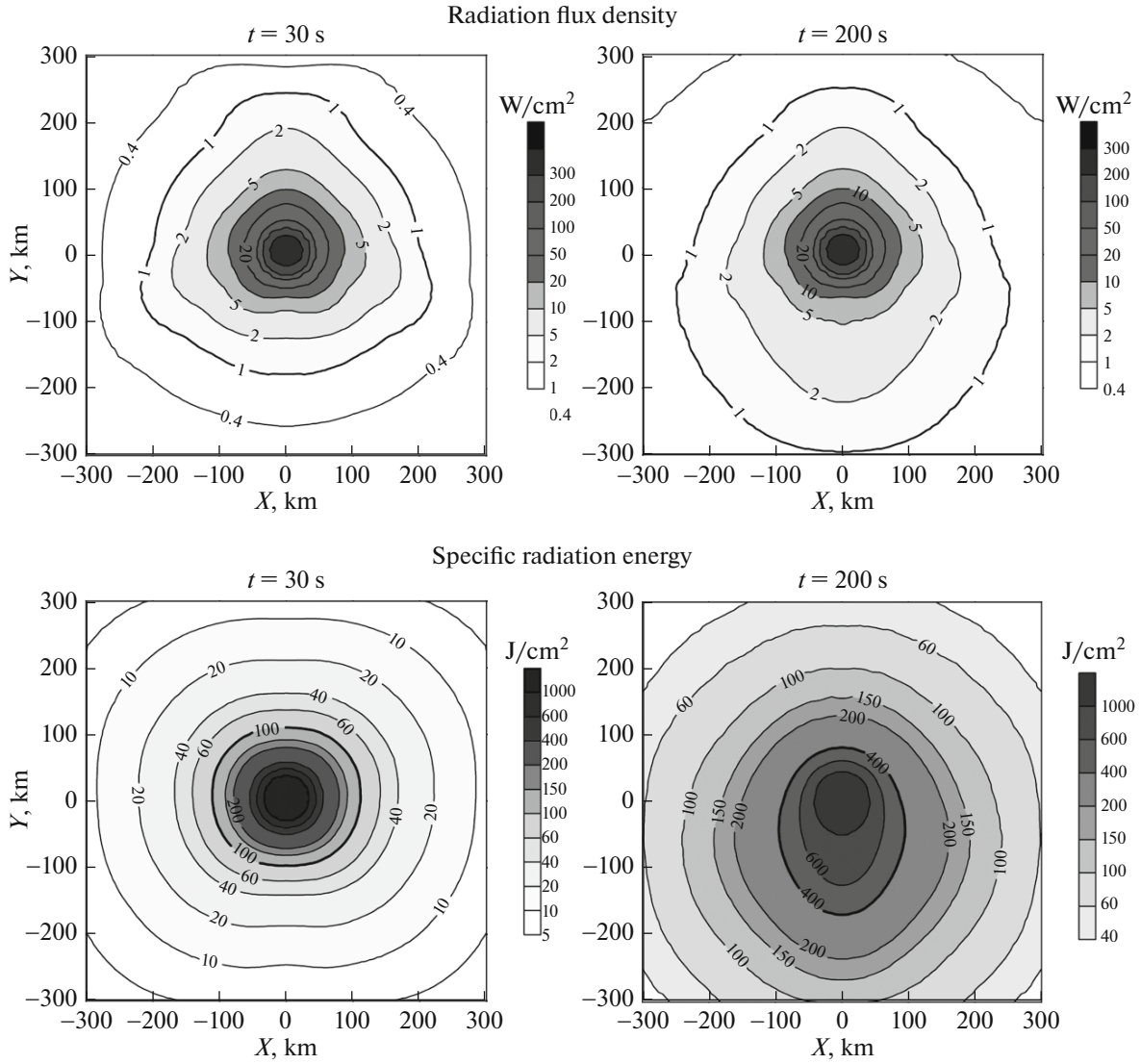

Fig. 10. Isolines of the radiation flux density and specific radiation energy on objects located on the Earth's surface and oriented at the radiation source for an impact of a 300-m asteroid at a velocity of 20 km/s at an angle of 45° to the surface at times of 30 and 100 s.

tion flux of 1 W/cm^2 given the same duration of exposure (Stoll and Chianta, 1969); and a level of 5–6 W/cm^2 is consistent with 1% lethality (Mannan and Lees, 2005). Thus, at distances within about 250 km, people may get second-degree burns, and at distances about 100 km lethal burns are possible.

Figure 10 shows the distribution of radiation fluxes and specific energy on the Earth's surface for an asteroid impact at an angle of 45°. In this case, the irradiation continues for about 200 s. According to (6), it requires a specific energy of 100 J/cm^2 for wood to ignite within 30 s and 400 J/cm^2 to ignite within 200 s (but by a weaker radiation flux). It turns out that a fire may arise over an area with a radius of about 100 km and individual outbreaks on an area with a radius of more than 150 km. At exposure times of 30–100 s, the threshold intensities for second- and third-degree burns are approximately 0.3–1.5 and 0.2–0.5 W/cm^2; thus, there is a hazard of skin burns in very clear weather in a zone with a radius of 200–300 km. The zone hazardous for human life (1% lethality) can be as large as 130–150 km.

If we consider the ignition of wood, the oblique impact leads to a certain increase in the area where there may be fires due to thermal radiation. This increase is lower than one could expect given the above-mentioned difference in radiation efficiency (~0.6 and ~4.5%) due to the nonlinear dependence of the threshold energy on the exposure time (long irradiation with a flux of lower intensity requires more energy). The human hazardous area increases more substantially.

CONCLUSIONS

As per our calculations, an impact by an Apophis-like asteroid (a stone body 300 meters in diameter at a velocity of 20 km/s) leads to serious regional (at distances of up to 300 km from the point of impact) consequences. Global consequences (at thousands of kilometers from the point of impact) are mainly due to ionospheric disturbances and, possibly, emissions of fine dust and vapor into the upper atmosphere.

Our scenario assumed that the asteroid density is 3.3 g/cm^3 and its size is 300 m. The lower density and larger size (1.9 g/cm^3 and 375 m as per the estimates by Müller et al. (2014) for the asteroid Apophis) increase the asteroid's initial energy by 10% (at the same velocity) and have almost no effect on the effective altitude of energy release (Shuvalov et al., 2016) and the scale of the possible consequences. Moreover, we considered a velocity of 20 km/s, which is close to the average velocity of impacts of stone bodies on the Earth (Ivanov, 2005). Apophis's velocity at atmospheric entry in the upcoming approaches is estimated at 12.6 km/s (http://neo.jpl.nasa.gov/risk/a99942.html); lower velocities at atmospheric entry for an asteroid of the same size and density result in lower deformation and fragmentation during the passage and a smaller size of the crater because of the lower impact velocity. A lower value of the initial kinetic energy leads to some reduction in the size of the areas affected by the impact hazards.

At flight path angles of 30°, 45°, and 90° to the Earth's surface, a 300-m asteroid approaches the surface in a largely deformed state, but undergoes virtually no deceleration in the atmosphere and no substantial fragmentation. The size and shape of the crater are almost the same as in the case of an Earth impact by a spherical asteroid.

The calculation of the overpressure and wind velocity on the Earth's surface due to an impact of a 300-m asteroid showed that the zone of destruction can be as large as 700–1000 km in diameter. The shape of the area where atmospheric overpressure exceeds a certain critical value varies with the magnitude of this critical value and with the flight path angle. A decrease in the path angle leads to a marked increase in the size of the zone of destruction.

The ionospheric disturbances from impacts of relatively large asteroids are global in nature and continue for hours. At distances of several thousand kilometers at altitudes of more than 100 km, air density disturbances are tens of percent and the vertical and horizontal velocity components are as high as hundreds of meters per second.

The radiation fluxes on the Earth's surface from an impact of a 300-m asteroid at angles of 45° and 90° to the Earth's surface were compared to show that the radiation pulse is much longer for the oblique impact than for the vertical one, 200 and ~30 s, respectively, but the fire zones are almost similar in size in a first approximation. In clear weather, the wood ignition zone may be as large as 200 km in diameter and that of individual fire outbreaks associated with ignition of flammable materials such as dry pine needles is 300–400 km in diameter. The central area of ~100 km in size is characterized by very heavy thermal damage, which is associated with the ignition of wood, roofs, clothes, etc. The human hazardous zone increases with decreasing flight path angle; people can feel thermal effects at distances of 250–400 km from the impact site.

Let us visualize what will happen if an asteroid of this size falls at the center of Moscow. The impact will create a crater encircling the entire historical part of Moscow inside the Sadovoe Koltso. On almost all the territory within the Koltsevaya road, all living beings will be killed by the shock wave. The entire territory of the Moscow oblast will be covered by massive fires. Destruction like that caused by the Chelyabinsk meteoroid event will be observed across the entire Central Federal District of Russia. Strong ionospheric disturbances capable of causing serious radio communication interrupts will be observed throughout Europe. Finally, abnormal weather phenomena will likely be observed throughout the world for a few years after the asteroid impact.

ACKNOWLEDGMENTS

This work was supported by the Russian Science Foundation, project no. 16-17-00107.

REFERENCES

Avilova, I.V., Biberman, L.M., Vorob'ev, V.S., Zamalin, V.M., Kobzev, G.A., Lagar'kov, A.N., Mnatsakanyan, A.Ks., *and Norman, G.E., Opticheskie svoistva goryachego vozdukha (Optic Properties of Hot Air)*, Moscow: Nauka, 1970.

Babrauskas, V., Ignition of wood: a review of the state of the art, *Proc. 9th Int. Fire Science and Engineering Conf. "Interflam 2001,"* London: Interscience Comm., 2001, pp. 71–88.

Babrauskas, V., *Ignition Handbook*, Issaquah, WA: Fire Sci., 2003.

Bancelin, F., Colas, W., Thuillot, D., Hestroffer, D., and Assafin, M., Asteroid (99942) Apophis: New predictions of Earth encounters for this potentially hazardous asteroid, *Astron. Astrophys.*, 2012, vol. 544, art. ID A15.

Binzel, R.P., Rivkin, A.S., Thomas, C.A., Vernazza, P., Burbine, T.H., DeMeo, F.E., Bus, S.J., Tokunaga, A.T., and Birlan, M., Spectral properties and composition of potentially hazardous asteroid (99942) Apophis, *Icarus*, 2009, vol. 200, no. 2, pp. 480–485.

Delbò, M., Cellino, A., and Tedesco, E.F., Albedo and size determination of potentially hazardous asteroids: (99942) Apophis, *Icarus*, 2007, vol. 188, no. 1, pp. 266–269.

Enaleev, R.Sh., Krasina, I.V., Gasilov, V.S., Chistov, Yu.S., and Tuchkova, O.A., Wood ignition, Vestn. Kazan. *Tekhnol. Univ.*, 2013, vol. 16, no. 10, pp. 99–106.

Filkov, A., Kuznetsov, V.T., and Guk, V.O., Ignition of wood subjected to dynamic radiant energy flux, in *Advances in Forest Fire Research*, Viegas, D.X., Ed., Coimbra: Univ. Coimbra, 2014, pp. 805–810.

Glasstone, S. and Dolan, P.J., *The Effects of Nuclear Weapons*, Washington, DC: U.S. Dep. Defense, Dep. Energy, 1977.

Grigoryan, S.S., Motion and destruction of meteorites in the planet's atmosphere, *Kosm. Issled.*, 1979, vol. 17, no. 6, pp. 875–893.

Grishin, A.M., Golovanov, A.N., and Medvedev, V.V., On the ignition of a layer of combustible forest materials by light radiation, *Combust., Explos. Shock Waves* (Engl. Transl.), 1999, vol. 35, no. 6, pp. 618–621.

Harris, A., Boslough, M., Chapman, C.R., Drube, L., Michel, P., and Harris, A., Asteroid impacts and modern civilization: Can we prevent a catastrophe? in *Asteroids IV*, Michel, P., DeMeo, F.E., and Bottke, W.P., Eds., Tucson: Univ. Arizona Press, 2015, pp. 867–886.

Herrick, R.R., Sharpton, V.L., Malin, M.C., Lyons, S.N., and Freely, K., Morphology and morphometry of impact craters, in *Venus II Geology, Geophysics, Atmosphere, and Solar Wind Environment*, Bougher, S.W., Hunten, D.M., and Phillips, R.J., Eds., Tucson: Univ. Arizona Press, 1997, pp. 1015–1046.

Hills, J.G. and Goda, M.P., The fragmentation of small asteroids in the atmosphere, *Astron. J.*, 1993, vol. 105, pp. 1114–1144.

Housen, KR. and Holsapple, K.A., Ejecta from impact craters, *Icarus*, 2011, vol. 211, pp. 856–875.

Ivanov, B.A., Distribution of impact craters and asteroids by size, in *Katastroficheskie vozdeistviya kosmicheskikh tel (Disastrous Effect of Space Bodies)*, Moscow: Akademkniga, 2005, pp. 62–77.

Ivanov, B.A. and Turtle, E.P., Modeling impact crater collapse acoustic fluidization implemented into a hydrocode, *XXXII Lunar and Planetary Science Conf., Abstracts of Papers*, Houston, TX, 2001, no. 1284.

Janssens, M., Piloted ignition of wood: a review, *Fire Mater.*, 1991, vol. 15, pp. 151–167.

Kosarev, I.B., Calculation of thermodynamic and optical properties of the vapors of cosmic bodies entering the earth's atmosphere, *J. Eng. Phys. Thermophys.*, 1999, vol. 72, no. 6, pp. 1030–1038.

Kosarev, I.B., The optical properties of vapors of matter of cosmic bodies invading the Earth atmosphere, *High Temp.*, 2009, vol. 47, no. 6, pp. 777–787.

Koschmieder, H., Theorie der horizontalen sichtweite II: Kontrast und sichtweite, *Beitr. Phys. Freien Atmos.*, 1925, vol. 12, pp. 171–181.

Kuznetsov, N.M., *Termodinamicheskie funktsii i udarnye adiabaty vozdukha pri vysokikh temperaturakh (Thermodynamic Functions and Impact Adiabats of Air at the High Temperatures)*, Moscow: Mashinostroenie, 1965.

Mannan, S. and Lees, F.P., *Lee's Loss Prevention in the Process Industries*, Vol. 1: *Hazard Identification, Assessment, and Control*, Amsterdam: Elsevier, 2005, 3rd ed.

McGetchin, T.R., Settle, M., and Head, J.W., Radial thickness variation in impact crater ejecta: Implications for lunar basin deposits, *Earth Planet. Sci. Lett.*, 1973, vol. 20, pp. 226–236.

McKinnon, W.B. and Schenk, P.M., Ejecta blanket scaling on the Moon and Mercury—inferences for projectile populations, *Proc. 16th Lunar and Planetary Science Conf., Abstracts of Papers*, Houston, TX, 1985, pp. 544–545.

Melosh, H.J., Hydrocode equation of state for SiO_2, *Meteorit. Planet. Sci.*, 2007, vol. 42, pp. 2079–2098.

Melosh, H.J. and Ivanov, B.A., Impact crater collapse, *Ann. Rev. Earth Planet. Sci.*, 1999, vol. 27, pp. 385–425.

Müller, T.G., Kiss, C., Scheirich, P., Pravec, P., O'Rourke, L., Vilenius, E., and Altieri, B., Thermal infrared observations of asteroid (99942) Apophis with Herschel, *Astron. Astrophys.*, 2014, vol. 566, art. ID A22.

Nemchinov, I.V., Svettsov, V.V., and Shuvalov, V.V., *Katastroficheskie vzaimodeistviya kosmicheskikh tel (The Disastrous Impact of Cosmic Bodies)*, Moscow: Akademkniga, 2005, pp. 12–61.

Pierazzo, E. and Melosh, H.J., Understanding oblique impacts from experiments, observations, and modeling, *Ann. Rev. Earth Planet. Sci.*, 2000, vol. 28, pp. 141–167.

Pittock, A.B., Ackerman, T.P., Crutzen, P.J., MacCracken, M.C., Shapiro, C.S., and Turco, R.P., *Environmental Consequences of Nuclear War (Scope 28)*, Vol. 1: *Physical and Atmospheric Effects*, Chichester: Wiley, 1986.

Popova, O.P., Jenniskens, P., Emel'yanenko, V., Emel'yanenko, V., Kartashova, A., Biryukov, E., Khaibrakhmanov, S., Shuvalov, V., Rybnov, Yu., Dudorov, A., Grokhovsky, V.I., Badyukov, D.D., Qing-Zhu Yin, Gural, P.S., Albers, J., et al., Chelyabinsk airburst, damage assessment, meteorite recovery, and characterization, *Science*, 2013, vol. 342, pp. 1069–1073.

Shuvalov, V.V., Multi-dimensional hydrodynamic code SOVA for interfacial flows: Application to thermal layer effect, *Shock Waves*, 1999, vol. 9, no. 6, pp. 381–390.

Shuvalov, V.V., Displacement of target material during impact cratering, in *Impact Markers in the Stratigraphic Record*, Berlin: Springer, 2003, pp. 121–135.

Shuvalov, V.V. and Artemieva, N.A., Numerical modeling of Tunguska-like impacts, *Planet. Space Sci.*, 2002, vol. 50/2, pp. 181–192.

Shuvalov, V. and Dypvik, H., Distribution of ejecta from small impact craters, *Meteorit. Planet. Sci.*, 2013, pp. 1–9. doi 10.1111/maps.12127

Shuvalov, V.V., Popova, O.P., Svettsov, V.V., Trubetskaya, I.A., and Glazachev, D.O., Determination of the height of the meteoric explosion, *Sol. Syst. Res.*, 2016, vol. 50, no. 1, pp. 1–12.

Shuvalov, V.V., Svettsov, V.V., and Trubetskaya, I.A., An estimate for the size of the area of damage on the Earth's surface after impacts of 10–300-m asteroids, *Sol. Syst. Res.*, 2013, vol. 47 (4), pp. 260–267.

Shuvalov, V.V. and Trubetskaya, I.A., Aerial bursts in the terrestrial atmosphere, *Sol. Syst. Res.*, 2007, vol. 41, no. 3, pp. 220–230.

Sokolov, L.L. and Kuteeva, G.A., Possible collision of Apophis asteroid after orbit verification, *Vestn. S.-Peterb. Gos. Univ., Ser. 1*, 2015, vol. 2 (60), no. 1, pp. 148–156.

Stoll, A.M. and Chianta, M.A., Method and rating system for evaluation of thermal protection, *Aerosp. Med.*, 1969, vol. 40, no. 11, pp. 1232–1238.

Svetsov, V.V., The low-cost numerical method for one-dimensional tasks in radiation gas dynamics, *Zh. Vychisl. Mat. Mat. Fiz.*, 1994a, vol. 34, no. 3, pp. 432–445.

Svetsov, V.V., Explosions in the lower and middle atmosphere: the spherically symmetrical stage, *Combust., Explos. Shock Waves* (Engl. Transl.), 1994b, vol. 30, no. 5, pp. 696–707.

Svetsov, V.V., Nemtchinov, I.V., and Teterev, A.V., Disintegration of large meteoroids in Earth's atmosphere: theoretical models, *Icarus*, 1995, vol. 116, no. 1, pp. 131–153.

Thompson, S.L. and Lauson, H.S., Improvements in the Chart D radiation hydrodynamic code III: Revised analytic equation of state, in *Report SC-RR-71 0714*, Albuquerque, NM: Sandia Natl. Lab., 1972.

Thuillot, W., Bancelin, D., Ivantsov, A., Desmars, J., Assafin, M., Eggl, S., Hestrofer, D., Rocher, P., Carry, B., David, P., Abe, L., Andreev, M., Arlot, J.-E., Asamil, A., Ayvasian, V., et al., The astrometric Gaia-FUNSSO observation campaign of 99942 Apophis, *Astron. Astrophys.*, 2015, vol. 583, art. ID A59.

Toon, O.B., Zahnle, K., Morrison, D., Turco, R.P., and Covey, C., Environmental perturbations caused by the impacts of asteroids and comets, *Rev. Geophys.*, 1997, vol. 35, no. 1, pp. 41–78.

Vasilyev, N.V., The Tunguska meteorite problem today, *Planet. Space Sci.*, 1998, vol. 46, nos. 2/3, pp. 129–150.

Vasilyev, N.V., *Tungusskii meteorit. Kosmicheskii fenomen leta 1908 (The Tunguska Meteorite: The Space Phenomenon of Summer 1908)*, Moscow: Russkaya Panorama, 2004.

Translated by A. Kobkova